Heterogeneous Catalysis

How to cite:
International Edition: doi.org/10.1002/anie.202110292
German Edition: doi.org/10.1002/ange.202110292

Single-Phase Formation of Rh_2O_3 Nanoparticles on h-BN Support for Highly Controlled Methane Partial Oxidation to Syngas

Younhwa Kim, Sungsu Kang, Dohun Kang, Kyung Rok Lee, Chyan Kyung Song, Jongbaek Sung, Ji Soo Kim, Hyunjoo Lee, Jungwon Park, and Jongheop Yi**

Abstract: *Single-phase formation of active metal oxides on supports has been vigorously pursued in many catalytic applications to suppress undesired reactions and to determine direct structure-property relationships. However, this is difficult to achieve in nanoscale range because the effect of non-uniform metal-support interfaces becomes dominant in the overall catalyst growth, leading to the nucleation of various metastable oxides. Herein, we develop a supported single-phase corundum-Rh_2O_3(I) nanocatalyst by utilizing controlled interaction between metal oxide and h-BN support. Atomic-resolution electron microscopy and first-principle calculation reveal that single-phase formation occurs via uniform and preferential attachment of Rh_2O_3(I) (110) seed planes on well-defined h-BN surface after decomposition of rhodium precursor. By utilizing the Rh/h-BN catalyst in methane partial oxidation, syngas is successfully produced solely following the direct route with keeping a H_2/CO ratio of 2, which makes it ideal for most downstream chemical processes.*

Introduction

Supported rhodium oxide nanocatalysts have been extensively utilized in various prominent reactions, especially in methane partial oxidation.[1] Impregnation and subsequent calcination procedures are the simplest and most widespread methods for synthesis of the supported catalysts, and metal oxide crystallites smaller than 10 nm are usually desired.[2] However, small nanoparticles exhibit a large surface-to-volume ratio, giving that inhomogeneous metal-support interfaces govern the overall nanoparticle growth during calcination.[3] More specifically, the anisotropic surface structure,[4] surface dangling bonds,[5] and intrinsic oxygen vacancies[6] on most oxide supports induce locally different energetic pathways, resulting in the formation of various rhodium oxide phases such as atomically dispersed RhO_x, disordered Rh_xO_y species, as well as corundum-Rh_2O_3(I) species, which is a thermodynamically stable phase below 1350 °C.[7] Such multiple active phases lead to the involvement of unwanted reactions in various catalytic applications,[8] making it difficult to identify the relationship between the structure and catalytic performance.

Colloidal synthesis using organic ligands and deposition methods is usually chosen to achieve uniformity of active metal species. However, it is difficult to completely remove the organic capping layers of the colloid nanoparticles by calcination, even at high temperatures (800 °C for 12 h),[9] and the well-defined nanostructures can be easily restructured during the ligand stripping process.[10] In addition, the growth of metal nanoparticles can be uniformly controlled in the nanospace of mesoporous materials.[11] Although their size can be controlled by adjusting the pore diameter, the inhomogeneous gas environment along the channel in the mesoporous materials results in the formation of various phases of the synthesized metal oxide.[12] Therefore, the key to achieving homogeneity of active metal-oxide species on supports for highly controlled reactions is to develop a fundamental synthetic strategy to ensure homogeneous metal-support interactions.

Inspired by the atomically isotropic surface properties of two-dimensional (2D) materials such as graphite and MoS_2,[13] 2D materials are potentially effective substrates for the synthesis of catalysts with homogeneously controlled active phases. However, these materials are unstable under high-temperature oxidative conditions,[14] and weak metal-2D support interaction leads to rapid particle agglomeration under harsh reaction conditions.[15] Hexagonal boron nitride (h-BN), which has a crystal structure similar to that of graphite, exhibits excellent chemical stability and thermal conductivity;[16] therefore, it has been recently utilized as a support for high-temperature oxidative reactions.[17] Importantly, monolayer h-BN sheets can be grown on various transition metal surfaces including a Rh (111) surface by forming a corrugated structure with a periodicity of ≈3 nm. This structure is called nanomesh[18] and is formed because of the strong Rh-N interaction that accommodates their lattice mismatch.[19] This system motivated us to utilize h-BN as a potential support to inversely control the growth of rhodium oxide nanoparticles.

[*] Y. Kim, S. Kang, D. Kang, K. R. Lee, Dr. C. K. Song, J. Sung, J. S. Kim, Prof. J. Park, Prof. J. Yi
School of Chemical and Biological Engineering, and Institute of Chemical Processes, Seoul National University
Seoul 08826 (Republic of Korea)
E-mail: jyi@snu.ac.kr
S. Kang, Prof. J. Park
Center for Nanoparticle Research, Institute of Basic Science (IBS)
Seoul 08826 (Republic of Korea)
E-mail: jungwonpark@snu.ac.kr
Prof. H. Lee
Department of Chemical and Biomolecular Engineering, Korea Advanced Institute of Science and Technology
Daejeon 305-701 (Republic of Korea)
Supporting information and the ORCID identification number(s) for the author(s) of this article can be found under: https://doi.org/10.1002/anie.202110292.

Herein, we develop a single-phase corundum-Rh_2O_3(I) nanocatalyst by exploiting the distinctive interaction between h-BN and rhodium oxide. A combination of atomic-resolution transmission electron microscopy (TEM) and first-principle calculations confirmed that the (110) seed plane of corundum-Rh_2O_3(I) is preferentially attached to the h-BN surface after decomposition of the rhodium nitrate precursor during calcination. The as-prepared h-BN supported single-phase Rh_2O_3(I) nanocatalyst was applied to catalytic methane partial oxidation (MPO; $CH_4 + 0.5\,O_2 \leftrightarrow CO + 2\,H_2$), a promising reaction for efficient methane transformation.[20] It is known that rhodium oxide catalysts are highly active in MPO, but their structural heterogeneity can lead to complex reaction mechanisms such as the desired direct route,[21] where CO and H_2 are the primary products, and the undesired indirect route,[22] where total methane oxidation produces CO_2 and H_2O, followed by steam- or dry-reforming with the remaining methane. By utilizing the Rh/h-BN catalyst, we achieved a highly controlled MPO process that produces syngas solely from the direct route with sustaining its superior catalytic activity. Moreover, we achieved high CO selectivity ($\approx 90\,\%$) with significantly reduced coke deposition in the isothermal methane reaction from chemical-looping MPO, which involves a redox reaction that uses the lattice oxygen of metal oxide for syngas generation. The highly controlled MPO from the single-phase rhodium oxide nanocatalyst contributes to the production of syngas with maintaining the H_2/CO ratio of 2, which is immediately suitable for most downstream chemical processes such as methanol and Fischer–Tropsch syntheses.

Results and Discussion

Characterization of supported rhodium oxide nanocatalysts

Rhodium oxide supported on h-BN catalysts (Rh/h-BN) was synthesized via a simple impregnation method using rhodium nitrate as a precursor followed by calcination at 600 °C for 5 h. For comparison, rhodium oxide catalysts on different supports with various specific surface areas (Rh/SiO_2, Rh/γ-Al_2O_3, Rh/Si_3N_4, Rh/ZrO_2, and Rh/TiO_2) were prepared using the same method (Table S1). No sharp peaks originating from bulk Rh_2O_3 species were observed and small rhodium oxide nanoparticles (most of them are below 5 nm in diameter) were formed on these supports, as shown in the XRD patterns and TEM images (Figure S1 and Figure S2). Hydrogen temperature-programed reduction (H_2-TPR) experiments were performed at 50–700 °C to investigate the reducibility of rhodium oxide species on the supports (Figure 1 a). The H_2-TPR profile of Rh/h-BN has a single symmetric peak centered at 146 °C, which is attributed to the reduction of Rh_2O_3 species located on the surface of the sample.[23] In contrast, H_2-TPR patterns of rhodium oxide catalysts on other supports have at least two peaks arising from disordered or dispersed rhodium oxide species, with

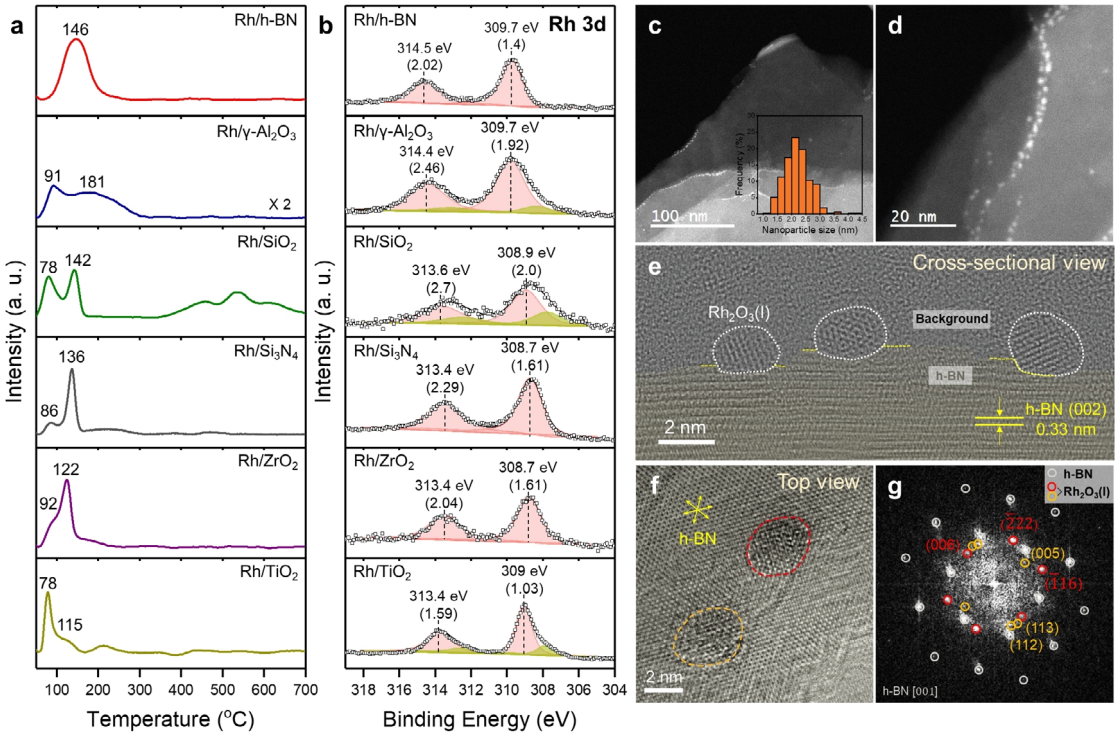

Figure 1. Ex situ characterization of supported rhodium oxide catalysts. a) H_2-TPR profiles and b) XPS Rh 3d spectra of Rh/h-BN, Rh/γ-Al_2O_3, Rh/SiO_2, Rh/Si_3N_4, Rh/ZrO_2, and Rh/TiO_2 calcined at 600 °C. c),d) TEM images of Rh/h-BN calcined at 600 °C; the size distribution (inset) is based on over 300 observed rhodium oxide nanoparticles. e) Cs-TEM cross-section image of a focused-ion-beam-processed specimen containing Rh/h-BN with a h-BN [002] zone axis. The region assigned to h-BN is indicated by overlaid pale-yellow-color. f) Top-view Cs-TEM image of Rh/h-BN; the red and yellow dashed circles indicate the Rh_2O_3 nanoparticles and g) the selected-area FFT pattern.

a low-temperature reduction peak located below 100 °C.[24] Moreover, the O/Rh ratio was obtained by quantifying the H_2 consumption, and the portion of easily reducible rhodium oxide species in the total rhodium species was calculated by deconvolution of the H_2-TPR profiles (Figure S3 and Table S2). Among the various supported catalysts, only Rh/h-BN shows an O/Rh ratio near 1.5, which corresponds to the stoichiometry of the Rh_2O_3 species. This indicates that a single Rh−O bond in the Rh_2O_3 species exists in Rh/h-BN after calcination at 600 °C, whereas various types of Rh−O bonds are formed on other supported catalysts. Notably, the single-phase formation of Rh_2O_3 species was also observed in Rh/h-BN catalysts with different weight percentages of rhodium (Figure S4 and Figure S5).

This single-phase characteristic of rhodium oxide species on Rh/h-BN can also be verified by the oxidation states of Rh in the supported catalysts, as measured by X-ray photoelectron spectroscopy (XPS). The XPS spectrum of Rh/h-BN shows higher binding energies of 314.5 eV (Rh^{3+} $3d_{3/2}$) and 309.7 eV (Rh^{3+} $3d_{5/2}$) with lowest full-width-at-half-maximum (FWHM) values of 2.02 and 1.4, respectively, as compared to other supported rhodium oxide catalysts, as shown in the XPS spectra and fitting results (Figure 1 b). This indicates that there is a single fully oxidized Rh^{3+} states from Rh_2O_3 species in Rh/h-BN. The lower binding energies of around 313 and 308 eV in Rh/γ-Al_2O_3, Rh/SiO_2, and Rh/TiO_2 indicate the presence of $Rh^{\delta+}$ ($0 < \delta < 3$) species, which correspond to the oxygen-deficient rhodium oxides.[25]

Scanning transmission electron microscopy (STEM images show the overall morphology of rhodium oxide nanoparticles on Rh/h-BN (Figure 1 c). The rhodium oxide nanoparticles in the as-synthesized Rh/h-BN have uniform size distribution with an average size of 2.20 nm ± 0.46, as shown in the inset of Figure 1 c. We confirmed that most of the rhodium nanoparticles were positioned on the h-BN surface nearby the boundaries between adjacent BN sheets, similar to other metal/2D support system,[26] as verified by the spherical aberration-corrected TEM (Cs-TEM) image of the cross-section of Rh/h-BN (Figure 1 e) and STEM image (Figure 1 d) with the absence of nanoparticles at the very edge of h-BN. According to the top-view Cs-TEM and selected fast Fourier transform (FFT) images (Figure 1 f,g), the rhodium oxide nanoparticles on Rh/h-BN clearly expose the lattice planes (−116)/(−222)/(006) and (112)/(113)/(005) of the corundum-Rh_2O_3(I) phase, respectively (Figure S6). Combining the results of H_2-TPR, XPS, and Cs-TEM/STEM, it is confirmed that the h-BN support enables the single-phase formation of corundum-Rh_2O_3(I) nanoparticles after calcination at 600 °C.

Preferential growth of corundum-Rh_2O_3(I) species on h-BN

We analyzed the structure of the rhodium oxide species at the early stage of calcination to elucidate the growth of single-phase Rh_2O_3(I) nanoparticles on h-BN. The temperature profile for the desorption of NO* species by decomposition of the rhodium nitrate precursor on h-BN shows a single maximum peak at around 300 °C, which indicates uniform interaction of the rhodium species with h-BN (Figure S7). In comparison, the desorption temperature profiles of other supports exhibit various maxima, indicating that the discrete metal-support interaction leads to various growth kinetics and the formation of metastable rhodium oxide phases as well as a thermodynamically stable Rh_2O_3(I) phase.

We investigated the crystallographic relationship between h-BN and rhodium oxide nanoparticles from Rh/h-BN calcined at a mild temperature of 300 °C, which resulted in the complete decomposition of rhodium nitrate, by using Cs-TEM. The regions containing Rh_2O_3 nanoparticles were separated from the h-BN region through an inverse FFT process by applying a mask filter to the original FFT patterns (Figure S8).

Notably, most of the rhodium oxide nanoparticles in the Cs-TEM image of Rh/h-BN calcined at 300 °C and in the selected FFT-converted images have a corundum-Rh_2O_3(I) [110] zone axis perpendicular to the underlying h-BN support (Figure 2 a–d). This indicates that the Rh_2O_3(I) (110) plane is preferentially attached to the surface of the h-BN support after decomposition of the rhodium nitrate. The Cs-STEM analysis of the Rh/h-BN calcined at 300 °C was conducted to determine the relative orientation of Rh_2O_3 nanoparticles to h-BN (Figure 2 e). The Rh_2O_3 nanoparticle in Rh/h-BN exposes the Rh_2O_3(I) (−224)/(006) plane with a Rh_2O_3(I) [110] zone axis, and the (006) plane is parallel to the (100) plane of h-BN. This angular relationship was also observed for other Rh_2O_3(I) nanoparticles supported on h-BN (Figure 2 f).

We conducted first-principle calculations to confirm that the (110) plane of corundum-Rh_2O_3(I) is the surface that preferentially interacts with the exposed surface of h-BN. The calculation results indicated that the Rh-terminated (110) surface of corundum-Rh_2O_3(I) most favorably interacts with the h-BN surface compared to the (001) and (012) planes (Figure 2 g). The calculated adhesion energy of the Rh_2O_3 (110) surfaces on h-BN (Rh_2O_3 (110)/h-BN) was −538 meV/BN, which is significantly lower (i.e. more negative) than the −254 meV/BN value, previously reported for h-BN/Rh (111) nanomesh[19] owing to the increased extent of Rh-N interactions. The equilibrium interlayer distance (height difference of the average position of bottom Rh and h-BN layers) is ≈2.25 Å, which is similar to the shortest Rh-N distance (2.21 Å) calculated for the h-BN/Rh(111) nanomesh.[19] The optimized atomic configuration of Rh_2O_3 (110)/h-BN along the *x*-direction shows that most of the Rh atoms in the first layer of corundum-Rh_2O_3(I) (110) are positioned near nitrogen sites of the h-BN surface with an average Rh−N bond distance of about 2.24 Å, which is shorter than the Rh−B bond distance (2.31 Å) (Figure 2 h, Figure S9 and Figure S10).

The charge density difference map, sliced by the second nitrogen sites of h-BN in Figure 2 h, indicates that charge accumulation was observed in the first Rh layer (Figure 2 i). The blue areas atop the N sites reveal that the displaced charge mainly originates from the N atoms. A Bader charge difference analysis also shows that the electrons are transferred from N to Rh atoms, which is compensated by those from B atoms (Figure S11). The accumulated charge in the Rh atoms is redistributed toward B sites on the h-BN surface and Rh atoms in the first layer of corundum-Rh_2O_3(I) (110), which is responsible for the spontaneous binding between

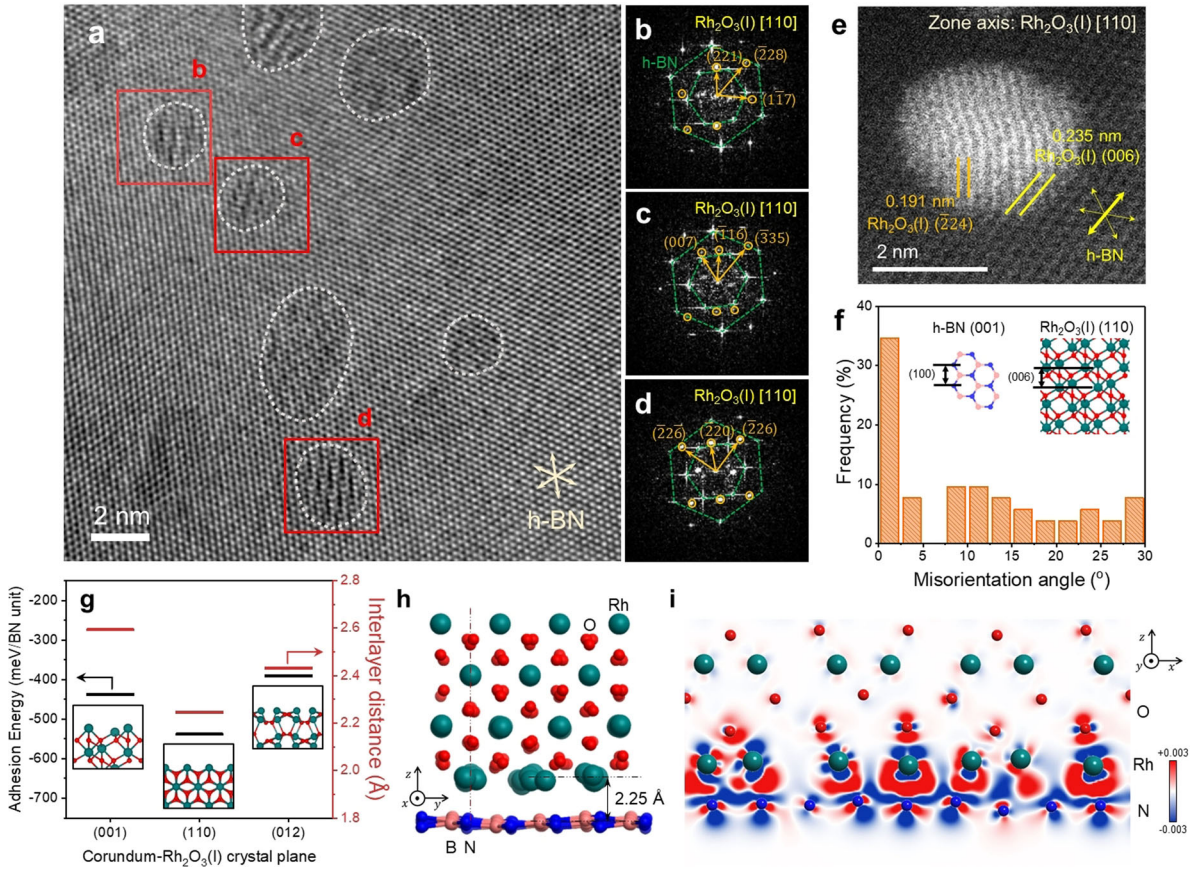

Figure 2. Preferential growth of corundum-Rh_2O_3(I) nanoparticles on h-BN. a) Cs-TEM image of Rh/h-BN calcined at 300 °C; the Rh_2O_3 nanoparticles outlined with dotted lines have a Rh_2O_3(I) [110] zone axis, and the Rh_2O_3 regions are distinguished from h-BN region through an inverse FFT process after applying a mask filter. b)–d) Selected-area FFT patterns of the Rh_2O_3 nanoparticles indicated in (a). e) Cs-STEM image of Rh/h-BN calcined at 300 °C. f) Histogram of misorientation angles between the (006) plane of corundum-Rh_2O_3(I) species and the (100) plane of h-BN. g) DFT-calculated adhesion energy and interlayer distance between optimized (001), (110), and (012) planes of the corundum-Rh_2O_3(I) phase and h-BN layer. h) Optimized atomic configuration of Rh_2O_3 (110)/h-BN from DFT calculations, and i) slice cutting of charge-density difference in Rh_2O_3 (110)/h-BN through the second N atoms. The range of the color map from blue to red corresponds to −0.003 to +0.003 e Å^{-3}, indicating electron depletion and accumulation, respectively.

Rh_2O_3 and h-BN. Therefore, the well-defined surface structure of h-BN and the large extent of Rh-N interactions contribute to the uniform stabilization of the Rh_2O_3 (110) seed plane after decomposition of the rhodium nitrate.

Effect of calcination temperatures on Rh_2O_3 and h-BN interaction

The 3D structure, preferentially grown on a 2D substrate, is usually degraded under high-temperature oxidative conditions because of the weak metal-support interaction and the instability of the supports under such harsh reaction conditions.[14] Severe aggregation of rhodium oxide species was also observed on the 2D graphene oxide and MoS_2 supports (Figure S12). In this regard, H_2-TPR, XPS, UV-visible-near-infrared (UV-vis-NIR) spectroscopy, and extended X-ray absorption fine structure (EXAFS) analysis of Rh/h-BN calcined at various temperatures was performed to analyze the structural stability of Rh_2O_3 nanoparticles with increasing calcination temperature. The H_2-TPR profile of Rh/h-BN calcined at 300 °C for 5 h shows a single reduction peak centered at 115 °C, which is assigned to the Rh_2O_3 species (Figure 3a). The single reduction peak was maintained with a shift toward higher temperatures as the calcination temperature increased, indicating an enhanced interaction between Rh_2O_3 species and h-BN.[27] Moreover, the surface rhodium species possess more electrons displaced from the h-BN support owing to their enhanced interaction,[28] as confirmed by the XPS spectra, wherein the binding energies of the Rh $3d_{5/2}$ and $3d_{3/2}$ peaks decrease at elevated calcination temperatures (Figure 3b). It is noteworthy that no sharp peak arising from Rh_2O_3 species was observed in the H_2-TPR patterns of rhodium oxide catalysts on other types of supports calcined at 300 °C (Figure S13). This observation implies that, on supports other than h-BN, uncontrolled seeds such as atomically dispersed or disordered rhodium oxide are formed at a mild calcination temperature of 300 °C, which agglomerate to form various rhodium oxide phases at higher calcination temperatures (to 600 °C).

UV-vis-NIR analysis of Rh/h-BN calcined at various temperatures for 5 h consistently confirmed the enhanced

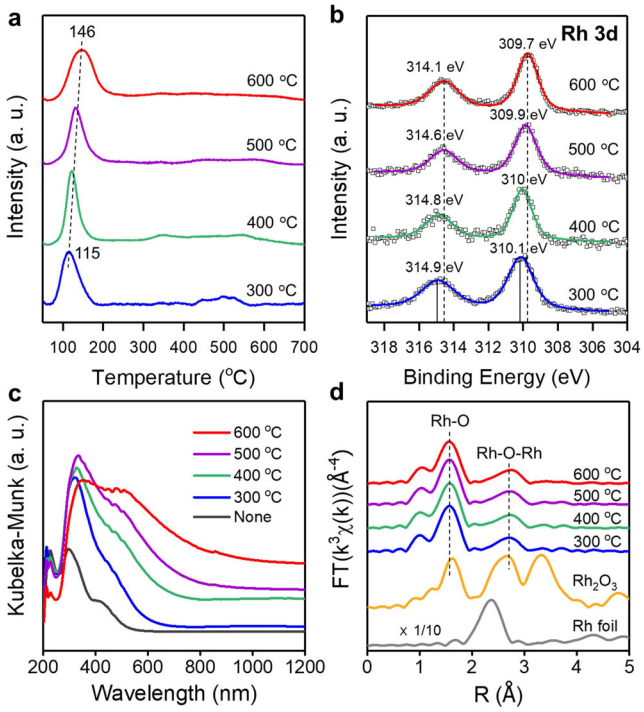

Figure 3. Effect of calcination temperatures on Rh/h-BN. a) H_2-TPR profiles, b) XPS Rh 3d spectra, and c) UV-vis-NIR spectra of Rh/h-BN calcined at 300, 400, 500, or 600 °C. d) Rh K-edge k^3-weighted FT-EXAFS spectra of Rh/h-BN calcined at various temperatures, bulk Rh_2O_3, and Rh foil.

interaction between Rh_2O_3 and h-BN as the calcination temperature increased (Figure 3c). The UV-vis-NIR spectra of Rh/h-BN calcined at 300 °C for 5 h showed two absorption bands centered at 320 and 450 nm corresponding to the allowed transitions $^1A_{1g} \rightarrow {}^1T_{1g}$ and $^1T_{2g}$ of the Rh^{3+} species.[29] These bands exhibited an evident red-shift, and the overall absorption intensity monotonously increased at elevated calcination temperatures, implying the incorporation of density of states between the valence and conduction bands of h-BN due to enhanced Rh_2O_3 and h-BN interactions.[30] The rhodium oxide species in Rh/h-BN, which were calcined at various temperatures for a short time (1 min), showed a negligible change in their Rh–O bond strength and their interaction with h-BN (Figure S14 and Figure S15). This implies that there is a prerequisite step for inducing stronger interactions between the Rh_2O_3 and h-BN supports. This can be attributed to the formation of oxidized boron species by the desorption of terminal B–OH and B–NH_2 groups from h-BN for bonding to rhodium species, as confirmed by in situ DRIFT and XPS analyses (Figure S16 and Figure S17). Such enhanced interactions with h-BN at high calcination temperatures are consistent with the results of previous studies.[17a,31] Instead, the components of Rh_2O_3 were well-sustained regardless of the calcination temperature, as confirmed by EXAFS analysis (Figure 3d). Therefore, the Rh_2O_3 (110) seed plane is stabilized after the decomposition of the rhodium nitrate precursor; thereafter, its interaction with h-BN is enhanced during calcination at elevated temperatures (up to 600 °C) and for an extended time, resulting in the formation of single-phase Rh_2O_3(I) species with uniform size distribution on the Rh/h-BN catalyst. Moreover, the enhanced interaction mainly contributes to the enhancement of catalytic stability, rather than the determination of reaction mechanisms (detailed in the following section).

Catalytic performance of supported rhodium oxide nanocatalysts and exploration of the reaction mechanism

The catalytic performance of the supported rhodium oxide nanocatalysts calcined at 600 °C was tested for MPO using a gas mixture of $CH_4/O_2/Ar = 4/2/94$ % to elucidate the advantages of single-phase formation of rhodium oxide nanoparticles on h-BN. The reaction over h-BN without rhodium deposition produced only CO_2, and the catalyst exhibited negligible activity up to 750 °C, demonstrating that the rhodium species play a major role in CO production (Figure S18). Among the supported catalysts, Rh/h-BN, Rh/γ-Al_2O_3, Rh/SiO_2, and Rh/Si_3N_4 showed high methane conversion rates and CO yields above 600 °C (Figure S19a, S19b, and Table S3). At 650 °C, Rh/h-BN showed a 72.5 % yield of CO, as good as that of one of the most active catalysts, Rh/γ-Al_2O_3, which produced a 69.5 % yield of CO under the same reaction conditions (Figure 4a). Moreover, the catalytic

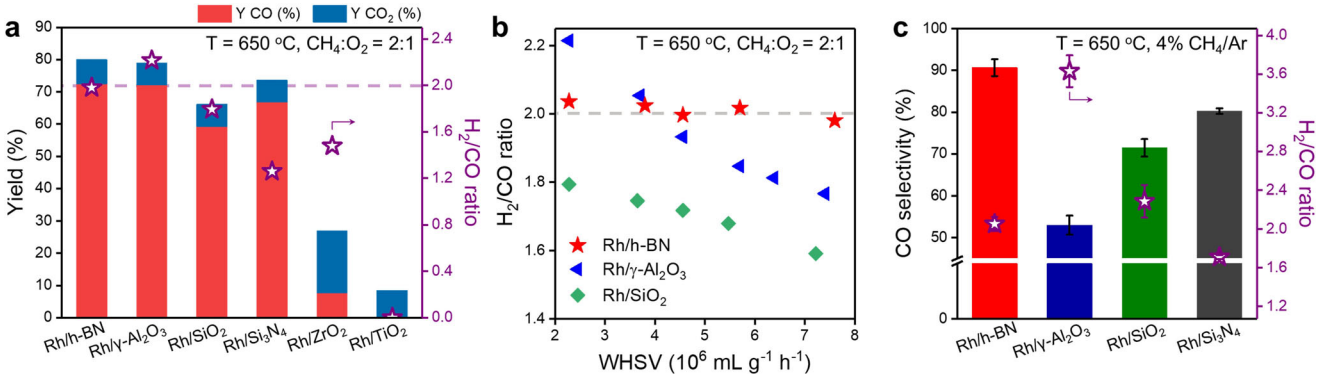

Figure 4. Catalytic performance of rhodium oxide nanocatalysts. a) MPO test at 650 °C over supported rhodium oxide catalysts (Feed: 4 % CH_4, 2 % O_2 with Ar balance, WHSV: 2280 $K g^{-1} h^{-1}$). b) H_2/CO ratio versus WHSV conditions for MPO at 650 °C over Rh/h-BN, Rh/γ-Al_2O_3, and Rh/SiO_2 catalysts. c) CO selectivity and H_2/CO ratio for CH_4 isothermal reaction at 650 °C over Rh/h-BN, Rh/γ-Al_2O_3, Rh/SiO_2, and Rh/Si_3N_4 catalysts.

stability of Rh/h-BN was enhanced by switching from low (400 °C) to high (600 °C) calcination temperatures because of the strengthened interaction between Rh_2O_3 and h-BN at elevated calcination temperatures (Figure S20). The Rh/h-BN calcined at 600 °C maintains 90 % of its initial activity after 70 h (Figure S21). The Rh/ZrO_2 catalyst exhibited a low CO yield of less than 10 %, and Rh/TiO_2 failed to produce CO. Note that only Rh/h-BN produced syngas with a H_2/CO ratio of 2 and showed a similar dependency of H_2 and CO yields on the reaction temperatures (Figure S19c), which explains the concurrent production of CO and H_2 from the MPO process. For the other supported rhodium oxide catalysts, the H_2/CO ratio is higher or lower than 2 and varies with the reaction temperature, indicating that the part of H_2 and CO is formed by different routes in MPO, such as an indirect route (total oxidation-methane reforming).

We focused on Rh/h-BN, Rh/γ-Al_2O_3, and Rh/SiO_2, which exhibited high methane conversion rates and selectivities toward syngas, and obtained the H_2/CO ratio at various weight hourly space velocities (WHSVs) to clarify the reaction pathway for H_2 and CO production (Figure 4b). If the direct conversion of methane to CO and H_2 was indeed the main route, these species would be formed simultaneously, and their yield profiles according to WHSV conditions would be identical.[32] Notably, we found that only the Rh/h-BN catalyst consistently maintained the H_2/CO production ratio of 2 under various WHSV conditions, while the others did not. With increasing WHSV, the methane conversion rate and syngas yield of all the supported rhodium oxide catalysts decreased owing to the short contact time with the reactants (Figure S22a–24a). For Rh/h-BN, the yield profiles of H_2 and CO under WHSV conditions were similar, whereas those for Rh/γ-Al_2O_3 and Rh/SiO_2 differ from each other (Figure S22b–24b). This observation demonstrates that corundum-Rh_2O_3(I) nanoparticles are the major active species for producing syngas via the direct route, and indeed, the formation of single-phase corundum-Rh_2O_3(I) on h-BN uniformly drives the direct route regardless of the WHSV conditions. Moreover, the direct route should produce syngas with high selectivity in the presence of O_2 because oxygen suppresses methane reforming from the indirect route.[33] In this regard, we confirmed that the Rh/h-BN can show high CO selectivity (69.9 %) and CO yield (57.8 %), as shown in Table S4. The Mars-Van Krevelen mechanism is suggested for direct syngas production: methane reduces the Rh_2O_3 species, which is reoxidized by oxygen gas.[34] The CH_4 pulse experiments and methane-oxygen injection cycling test showed that the lattice oxygen of the Rh_2O_3(I) species in Rh/h-BN is used directly in CO production (Figure S25 and Figure S26).

The single-phase Rh_2O_3(I) species in Rh/h-BN catalysts is also significantly effective in chemical-looping MPO. The primary function of rhodium oxide species on various supports was evaluated by quantifying the products, including H_2, CO, and CO_2, and by considering the amount of deposited carbon during the methane isothermal reaction (Figure 4c, Figure S27, and Table S5). Importantly, Rh/h-BN exhibited a superior CO selectivity (≈90 %) and an average H_2/CO ratio of 2.1, which is close to the theoretical value of direct MPO. In comparison, Rh/γ-Al_2O_3, Rh/SiO_2, and Rh/Si_3N_4 catalysts showed low CO selectivity due to coke formation, and the average H_2/CO ratio was higher or lower than 2. These results reveal that different Rh species in Rh/γ-Al_2O_3, Rh/SiO_2, and Rh/Si_3N_4 catalysts induce deep decomposition of methane and coke formation after the isothermal methane reaction.

We investigated the transient responses of the products from MPO over Rh/h-BN, Rh/γ-Al_2O_3, Rh/SiO_2, and Rh/Si_3N_4 by pulse experiments to confirm whether total oxidation is triggered before CO production; if so, an indirect route is implied.[35] After injecting CH_4 and O_2 pulses into the sample at 650 °C, the products CO and CO_2 were monitored using an online mass spectrometer (Figure 5a). The maximum intensities of CO and CO_2 were concurrently detected in MPO over Rh/h-BN. In contrast, a part of the CO_2 was detected earlier than CO over Rh/γ-Al_2O_3, Rh/SiO_2, and Rh/Si_3N_4 catalysts, demonstrating that CO_2 was initially formed from CH_4 before CO production. At 650 °C, the catalysts, including Rh/h-BN, showed a similar CO selectivity toward MPO, as confirmed in Figure 4a. In this regard, some CO is produced

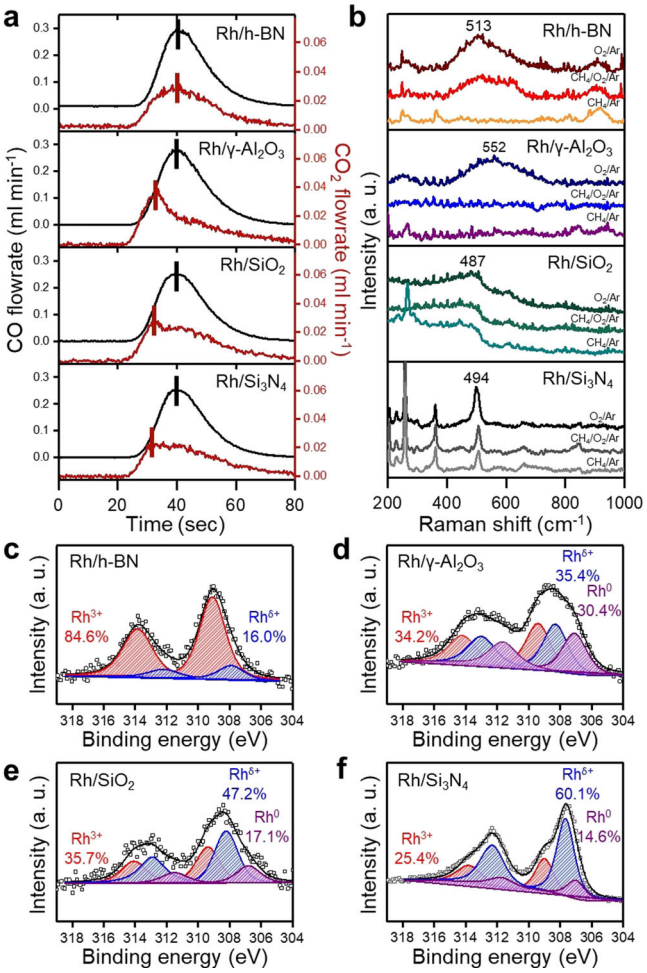

Figure 5. a) Transient responses of CO and CO_2 after pulsing CH_4/O_2 at a feed molar ratio of 2 at 650 °C over Rh/h-BN, Rh/γ-Al_2O_3, Rh/SiO_2, and Rh/Si_3N_4. b) In situ Raman spectra of Rh/h-BN, Rh/γ-Al_2O_3, Rh/SiO_2, and Rh/Si_3N_4 at 650 °C under 5 % O_2/Ar, subsequent 10 % CH_4/5 % O_2/Ar, and 10 % CH_4/Ar flow. c)–f) Ex situ XPS Rh 3d spectra of Rh/h-BN, Rh/γ-Al_2O_3, Rh/SiO_2, and Rh/Si_3N_4 after MPO at 650 °C.

via an indirect route over Rh/γ-Al_2O_3, Rh/SiO_2, and Rh/Si_3N_4 catalysts.

The oxidation state of rhodium species during MPO is strongly related to the reaction pathway for syngas production.[34,36] During the MPO process, metallic rhodium species lead to syngas production via methane reforming.[36a] Moreover, metallic species can lead to the decomposition of CH_4 and coke formation during the isothermal methane reaction.[37] The changes in the Rh−O bonds of Rh/h-BN, Rh/SiO_2, Rh/γ-Al_2O_3, and Rh/Si_3N_4 during MPO were investigated by in situ Raman spectroscopy (Figure 5b). The broad bands centered at 400–600 cm^{-1} were assigned to the Rh-O symmetric stretch of rhodium oxide.[38] Under a flow of 5% O_2/Ar at 650 °C, all the samples contained Rh−O bonds originating from the rhodium oxide species.

Notably, the intensity of the Rh−O bond at 513 cm^{-1} for Rh/h-BN slightly decreased, but still existed in oxidized states under 10% CH_4/5% O_2/Ar flow. In comparison, the intensity of the Rh-O stretch for the other supported catalysts was below the detection level of Raman spectroscopy during the reaction. Therefore, the electronic properties of the supported rhodium catalysts after MPO were further investigated by ex situ XPS analysis (Figure 5c–f). The spectra showed that the rhodium species from Rh/h-BN were in oxidized states, which is consistent with the Raman analysis results. However, Rh/γ-Al_2O_3, Rh/SiO_2, and Rh/Si_3N_4 contained metallic rhodium species, as well as partially oxidized rhodium species, after the MPO reaction. As confirmed by the H_2-TPR results in Figure 1a, the dispersed or disordered rhodium oxide species on Rh/γ-Al_2O_3, Rh/SiO_2, and Rh/Si_3N_4 could be easily reduced because of the weak Rh−O bond strength. Therefore, these rhodium oxide species were converted into their metallic states during the MPO process, resulting in an indirect route for syngas production in MPO and excess carbon deposition in the isothermal methane reaction of chemical-looping MPO.

Conclusion

In this study, we show that h-BN support induces the single-phase formation of corundum-Rh_2O_3(I) nanocatalysts owing to the preferential attachment of the Rh_2O_3(I) (110) seed plane on the h-BN surface after decomposition of the rhodium precursor. After that, the interaction between Rh_2O_3 nanoparticles and the h-BN support is getting stronger at elevated calcination temperatures with sustaining the Rh_2O_3 components, imparting enhanced catalytic stability. The catalytic MPO over Rh/h-BN occurs solely via the direct route owing to the single-phase active Rh_2O_3 species on h-BN. In addition, Rh/h-BN shows a high CO selectivity ($\approx$90%) for the isothermal methane reaction. These highly controlled, direct MPOs from Rh/h-BN are ideal for applying to downstream chemical processes, which require a H_2/CO ratio of $\approx$2 for synthesizing value-added chemicals. Furthermore, supported metal-oxide nanocatalysts have been extensively utilized in various areas, such as electrocatalysis,[39] photocatalysis,[40] and thermocatalysis,[41] and control of the metal nanoparticle-support interaction has recently received considerable attention for controlling the reaction pathway.[42] Our results highlight the importance of understanding the distinctive metal-support interactions at the nanoscale for synthesizing single-phase catalysts, which can be applied to various heterogeneous reactions for highly controlled catalytic activity and for determining the catalytic structure-property relationships.

Acknowledgements

This work was supported by the C1 Gas Refinery Program through the National Research Foundation of Korea (NRF) funded by the Ministry of Science, ICT and Future Planning (2015M3D3A1A01064899). This work was also supported by a NRF grant funded by the Korean Government (NRF-2016-Fostering Core Leaders of the Future Basic Science Program/Global PhD Fellowship Program). J.P. acknowledges the financial support from the Institute for Basic Science (IBS-R006-D1) and the NRF grant funded by the Korean Government (NRF-2017R1A5A1015365 and NRF-2019M3E6A1064877). The experiments at PLS were supported by POSTECH.

Conflict of Interest

The authors declare no conflict of interest.

Keywords: heterogeneous catalysis · hexagonal boron nitride · methane · rhodium oxide · syngas

[1] a) D. M. Ligthart, R. A. van Santen, E. J. Hensen, *Angew. Chem. Int. Ed.* **2011**, *50*, 5306–5310; *Angew. Chem.* **2011**, *123*, 5418–5422; b) H. Asakura, S. Hosokawa, T. Ina, K. Kato, K. Nitta, K. Uera, T. Uruga, H. Miura, T. Shishido, J. Ohyama, *J. Am. Chem. Soc.* **2018**, *140*, 176–184; c) C. Italiano, N. Luchters, L. Pino, J. Fletcher, S. Specchia, J. Fletcher, A. Vita, *Int. J. Hydrogen Energy* **2018**, *43*, 11755–11765; d) C. Au, H. Wang, *J. Catal.* **1997**, *167*, 337–345; e) E. Ruckenstein, H. Wang, *J. Catal.* **2000**, *190*, 32–38.

[2] P. Munnik, P. E. de Jongh, K. P. de Jong, *Chem. Rev.* **2015**, *115*, 6687–6718.

[3] a) V. Esposito, I. E. Castelli, *Adv. Mater. Interfaces* **2020**, *7*, 1902090; b) Z.-c. Zhang, B. Xu, X. Wang, *Chem. Soc. Rev.* **2014**, *43*, 7870–7886; c) A. Y. Stakheev, L. Kustov, *Appl. Catal. A* **1999**, *188*, 3–35.

[4] H. Miyata, W. Kubo, A. Sakai, Y. Ishida, T. Noma, M. Watanabe, A. Bendavid, P. J. Martin, *J. Am. Chem. Soc.* **2010**, *132*, 9414–9419.

[5] A. L. Schoenhalz, G. M. Dalpian, *J. Nanopart. Res.* **2012**, *14*, 1162.

[6] J. Li, Z. Liu, D. A. Cullen, W. Hu, J. Huang, L. Yao, Z. Peng, P. Liao, R. Wang, *ACS Catal.* **2019**, *9*, 11088–11103.

[7] a) Z. Weng-Sieh, R. Gronsky, A. T. Bell, *J. Catal.* **1998**, *174*, 22–33; b) Z. Weng-Sieh, R. Gronsky, A. T. Bell, *J. Catal.* **1997**, *170*, 62–74; c) C.-P. Hwang, C.-T. Yeh, Q. Zhu, *Catal. Today* **1999**, *51*, 93–101.

[8] a) C. Asokan, Y. Yang, A. Dang, A. B. Getsoian, P. Christopher, *ACS Catal.* **2020**, *10*, 5217–5222; b) R. Duarte, F. Krumeich, J. A. van Bokhoven, *ACS Catal.* **2014**, *4*, 1279–1286.

[9] P. Mohapatra, S. Shaw, D. Mendivelso-Perez, J. M. Bobbitt, T. F. Silva, F. Naab, B. Yuan, X. Tian, E. A. Smith, L. Cademartiri, *Nat. Commun.* **2017**, *8*, 1 – 7.
[10] L. M. Rossi, J. L. Fiorio, M. A. Garcia, C. P. Ferraz, *Dalton Trans.* **2018**, *47*, 5889 – 5915.
[11] S. Singh, R. Kumar, H. D. Setiabudi, S. Nanda, D.-V. N. Vo, *Appl. Catal. A* **2018**, *559*, 57 – 74.
[12] a) F. Yin, S. Ji, P. Wu, F. Zhao, C. Li, *J. Catal.* **2008**, *257*, 108 – 116; b) I. Yuranov, L. Kiwi-Minsker, P. Buffat, A. Renken, *Chem. Mater.* **2004**, *16*, 760 – 761.
[13] J. Yang, K. Kim, Y. Lee, K. Kim, W. C. Lee, J. Park, *FlatChem* **2017**, *5*, 50 – 68.
[14] a) L. Xiaowei, R. Jean-Charles, Y. Suyuan, *Nucl. Eng. Des.* **2004**, *227*, 273 – 280; b) K. H. Hu, X. G. Hu, X. J. Sun, *Appl. Surf. Sci.* **2010**, *256*, 2517 – 2523.
[15] H. Ma, H. Wang, P. C. Burns, B. K. McNamara, E. C. Buck, C. Na, *J. Nucl. Mater.* **2016**, *475*, 113 – 122.
[16] a) Q. Weng, X. Wang, X. Wang, Y. Bando, D. Golberg, *Chem. Soc. Rev.* **2016**, *45*, 3989 – 4012; b) Z. Liu, Y. Gong, W. Zhou, L. Ma, J. Yu, J. C. Idrobo, J. Jung, A. H. MacDonald, R. Vajtai, J. Lou, *Nat. Commun.* **2013**, *4*, 1 – 8.
[17] a) J. Dong, Q. Fu, H. Li, J. Xiao, B. Yang, B. Zhang, Y. Bai, T. Song, R. Zhang, L. Gao, *J. Am. Chem. Soc.* **2020**, *142*, 17167 – 17174; b) Z. Zhang, J. Su, A. S. Matias, M. Gordon, Y.-S. Liu, J. Guo, C. Song, C. Dun, D. Prendergast, G. A. Somorjai, *Proc. Natl. Acad. Sci. USA* **2020**, *117*, 29442 – 29452; c) Y.-R. Liu, X. Li, W.-M. Liao, A.-P. Jia, Y.-J. Wang, M.-F. Luo, J.-Q. Lu, *ACS Catal.* **2019**, *9*, 1472 – 1481.
[18] a) M. Kim, S. W. Moon, G. Kim, S. I. Yoon, K. C. Kim, S. K. Min, H. S. Shin, *Chem. Mater.* **2020**, *32*, 4584 – 4590; b) W. Auwärter, *Surf. Sci. Rep.* **2019**, *74*, 1 – 95; c) M. Corso, W. Auwärter, M. Muntwiler, A. Tamai, T. Greber, J. Osterwalder, *Science* **2004**, *303*, 217 – 220; d) A. Gibb, N. Alem, A. Zettl, *Phys. Status Solidi B* **2013**, *250*, 2727 – 2731.
[19] J. G. Diaz, Y. Ding, R. Koitz, A. P. Seitsonen, M. Iannuzzi, J. Hutter, *Theor. Chem. Acc.* **2013**, *132*, 1350.
[20] a) B. C. Enger, R. Lødeng, A. Holmen, *Appl. Catal. A* **2008**, *346*, 1 – 27; b) P. Arku, B. Regmi, A. Dutta, *Chem. Eng. Res. Des.* **2018**, *136*, 385 – 402.
[21] a) P. Torniainen, X. Chu, L. Schmidt, *J. Catal.* **1994**, *146*, 1 – 10; b) D. Hickman, L. D. Schmidt, *J. Catal.* **1992**, *138*, 267 – 282.
[22] a) J. Slaa, R. Berger, G. Marin, *Catal. Lett.* **1997**, *43*, 63 – 70; b) I. Tavazzi, A. Beretta, G. Groppi, P. Forzatti, *J. Catal.* **2006**, *241*, 1 – 13.
[23] C. Wong, R. W. McCabe, *J. Catal.* **1987**, *107*, 535 – 547.
[24] W. Z. Weng, C. R. Luo, J. J. Huang, Y. Y. Liao, H. L. Wan, *Top. Catal.* **2003**, *22*, 87 – 93.
[25] Y. Wang, Z. Song, D. Ma, H. Luo, D. Liang, X. Bao, *J. Mol. Catal. A* **1999**, *149*, 51 – 61.
[26] a) J. E. Johns, J. M. Alaboson, S. Patwardhan, C. R. Ryder, G. C. Schatz, M. C. Hersam, *J. Am. Chem. Soc.* **2013**, *135*, 18121 – 18125; b) A. Cavallin, M. Pozzo, C. Africh, A. Baraldi, E. Vesselli, C. Dri, G. Comelli, R. Larciprete, P. Lacovig, S. Lizzit, *ACS Nano* **2012**, *6*, 3034 – 3043.
[27] M. Xu, S. He, H. Chen, G. Cui, L. Zheng, B. Wang, M. Wei, *ACS Catal.* **2017**, *7*, 7600 – 7609.
[28] J. Ohyama, A. Yamamoto, K. Teramura, T. Shishido, T. Tanaka, *ACS Catal.* **2011**, *1*, 187 – 192.
[29] Q. Lin, K.-i. Shimizu, A. Satsuma, *Appl. Catal. A* **2012**, *419*, 142 – 147.
[30] T. Bugrova, T. Kharlamova, V. Svetlichnyi, A. Savel'eva, M. Salaev, G. Mamontov, *Catal. Today* **2021**, *375*, 36 – 47.
[31] T. Song, J. Dong, R. Li, X. Xu, M. Hiroaki, B. Yang, R. Zhang, Y. Bai, H. Xin, L. Lin, *J. Phys. Chem. Lett.* **2021**, *12*, 4187 – 4194.
[32] V. A. Kondratenko, C. Berger-Karin, E. V. Kondratenko, *ACS Catal.* **2014**, *4*, 3136 – 3144.
[33] a) Y. Boucouvalas, Z. Zhang, X. E. Verykios, *Catal. Lett.* **1996**, *40*, 189 – 195; b) D. Dissanayake, M. P. Rosynek, K. C. Kharas, J. H. Lunsford, *J. Catal.* **1991**, *132*, 117 – 127.
[34] E. Mallens, J. Hoebink, G. Marin, *J. Catal.* **1997**, *167*, 43 – 56.
[35] M. D. Salazar-Villalpando, D. A. Berry, T. H. Gardner, *Int. J. Hydrogen Energy* **2008**, *33*, 2695 – 2703.
[36] a) J.-D. Grunwaldt, S. Hannemann, C. G. Schroer, A. Baiker, *J. Phys. Chem. B* **2006**, *110*, 8674 – 8680; b) Z. Tian, O. Dewaele, G. B. Marin, *Catal. Lett.* **1999**, *57*, 9 – 17.
[37] A. Mishra, R. Dudek, A. Gaffney, D. Ding, F. Li, *Catal. Today* DOI: 10.1016/j.cattod.2019.09.010.
[38] a) C. T. Williams, K.-Y. Chen, C. G. Takoudis, M. J. Weaver, *J. Phys. Chem. B* **1998**, *102*, 4785 – 4794; b) A. A. Tolia, R. Smiley, W. Delgass, C. G. Takoudis, M. J. Weaver, *J. Catal.* **1994**, *150*, 56 – 70.
[39] K. Jin, J. H. Maalouf, N. Lazouski, N. Corbin, D. Yang, K. Manthiram, *J. Am. Chem. Soc.* **2019**, *141*, 6413 – 6418.
[40] D. Barreca, G. Carraro, V. Gombac, A. Gasparotto, C. Maccato, P. Fornasiero, E. Tondello, *Adv. Funct. Mater.* **2011**, *21*, 2611 – 2623.
[41] a) Y. Kim, T. Y. Kim, C. K. Song, K. R. Lee, S. Bae, H. Park, D. Yun, Y. S. Yun, I. Nam, J. Park, *Nano Energy* **2020**, 105704; b) T. A. Le, M. S. Kim, S. H. Lee, T. W. Kim, E. D. Park, *Catal. Today* **2017**, *293*, 89 – 96.
[42] a) T. W. van Deelen, C. H. Mejía, K. P. de Jong, *Nat. Catal.* **2019**, *2*, 955; b) H. Ha, S. Yoon, K. An, H. Y. Kim, *ACS Catal.* **2018**, *8*, 11491 – 11501; c) K. Murata, Y. Mahara, J. Ohyama, Y. Yamamoto, S. Arai, A. Satsuma, *Angew. Chem. Int. Ed.* **2017**, *56*, 15993 – 15997; *Angew. Chem.* **2017**, *129*, 16209 – 16213.

Manuscript received: August 2, 2021
Accepted manuscript online: September 15, 2021
Version of record online: ■■ ■■, ■■■■

Research Articles

Heterogeneous Catalysis

Y. Kim, S. Kang, D. Kang, K. R. Lee, C. K. Song, J. Sung, J. S. Kim, H. Lee, J. Park,* J. Yi* _____ ■■■■–■■■■

Single-Phase Formation of Rh_2O_3 Nanoparticles on h-BN Support for Highly Controlled Methane Partial Oxidation to Syngas

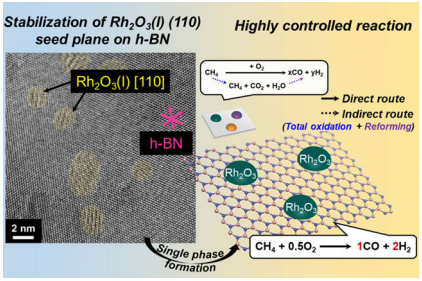

A single-phase Rh_2O_3 nanocatalyst is developed by exploiting the stabilization of the (110) plane of the Rh_2O_3(I) seed on hexagonal boron nitride (h-BN) after decomposition of the rhodium precursor. By using the Rh/h-BN, catalytic methane partial oxidation to syngas was accomplished solely via the direct route.